CORRECTED 11 FEBRUARY 2026; SEE LAST PAGE
SCIENCE ROBOTICS | RESEARCH ARTICLE

BIOMIMETICS

Energy efficiency and neural control of continuous versus intermittent swimming in a fishlike robot

Xiangxiao Liu[1]*, François A. Longchamp[1], Luca Zunino[1], Louis Gevers[1], Lisa R. Schneider[1], Selina I. Bothner[1], André Guignard[1], Alessandro Crespi[1], Guillaume Bellegarda[1], Alexandre Bernardino[2], Eva A. Naumann[3], Auke J. Ijspeert[1]*

Many aquatic animals, including larval zebrafish, exhibit intermittent locomotion, moving via discrete swimming bouts followed by passive glides rather than continuous movement. However, fundamental questions remain unresolved: What neural mechanisms drive this behavior, and what functional benefits does this behavior offer? Specifically, is intermittent swimming more energy efficient than continuous swimming, and, if so, by what mechanism? Live-animal experiments pose technical challenges, because observing or manipulating internal physiological states in freely swimming animals is difficult. Hence, we developed ZBot, a bioinspired robot that replicates the morphological features of larval zebrafish. Embedding a network model inspired by neural circuits and kinematic recordings of larval zebrafish, ZBot reproduces diverse swimming gaits of larval zebrafish bout-and-glide locomotion. By testing ZBot swimming in both turbulent and viscous flow regimes, we confirm that viscous flow markedly reduces traveled distance but minimally affects turning angles. We further tested ZBot in these regimes to analyze how key parameters (tail-beating frequency and amplitude) influence velocity and power use. Our results show that intermittent swimming lowers the energetic cost of transport across most achievable velocities in both flow regimes. Although prior work linked this efficiency to fluid dynamics, like reduced glide drag, we identify an extra mechanism: better actuator efficiency. Mechanistically, this benefit arises because intermittent locomotion shifts the robot's actuators to higher inherent efficiency. This work introduces a fishlike robot capable of biomimetic intermittent swimming—with demonstrated energy advantages at relevant speeds—and provides general insights into the factors shaping locomotor behavior and efficiency in aquatic animals.

INTRODUCTION

Bioinspired robots are valuable tools for investigating adaptive animal behaviors, including locomotion and sensory processing. They allow researchers to embody neural mechanisms and systematically study their effects under conditions analogous to natural systems (*1*, *2*). Zebrafish larvae, in particular, have emerged as a popular model for studying adaptive behaviors, such as swimming and sensory processing, because of experimental advantages like transparency, small brain size, ease of behavioral measurement, and tractable genetic manipulation (*3*, *4*). Mapping of their brainwide neural activity has further uncovered key details about the neural circuits and mechanisms governing locomotion (*4*–*6*). Although previous zebrafish-inspired robots have been developed (*7*–*10*), to the best of our knowledge, none integrate sensors or neural mechanisms—a critical gap that limits systematic exploration of how these components drive behavior. To fulfill this need, we created a larval zebrafish–inspired robot, ZBot, that incorporates sensors including wattmeters and cameras. We designed ZBot to serve as a platform for studying the parameters controlling locomotion behaviors, to test hypothesized neural mechanisms, and to evaluate how these mechanisms shape the ZBot's behavior through interactions with its body and environment.

Bout-and-glide swimming, also termed burst-and-coast or beat-and-glide swimming, is a widespread intermittent locomotion strategy observed across diverse aquatic organisms, including larval fish (*4*, *11*, *12*), tuna (*13*), koi carp (*14*), red-nose tetra (*15*), and whales (*16*, *17*). It is characterized by brief periods of body and tail undulations followed by a passive gliding phase with a straight posture (*11*, *18*). Biological studies on zebrafish have identified partial neural mechanisms underlying this swimming mode, such as spinal cord central pattern generators (CPGs) that produce rhythmic tail movements and a supraspinal gating center that initiates CPG activation (*4*, *19*). However, efforts to model the neural mechanisms driving bout-and-glide swimming remain limited (*20*), and investigations of the effects of neural circuits on swimming behaviors with simulations or robots are missing.

Aquatic animals that exhibit bout-and-glide swimming span a wide range of body sizes, from small larval fish swimming in intermediate or viscous regimes with relatively low Reynolds (*Re*) numbers to large koi carp, tuna, and whales swimming in turbulent flow regimes with high *Re* numbers (*21*–*25*). However, the influence of different hydrodynamic conditions on dynamic behavior during bout-and-glide swimming remains unknown. A key technical challenge in studying how size-related hydrodynamic conditions affect ZBot's swimming is that drastically altering the robot's body size while preserving other parameters like actuation and neural control is impossible.

Potential explanations have been proposed for why some fish use intermittent instead of continuous swimming. One potential explanation is that intermittent swimming improves perception because of stabilized heading during gliding (*26*). Another is that intermittent swimming improves the energy efficiency of swimming. The leading hypothesis is that bout-and-glide swimming enhances energy transfer from kinematic tail movements to the dynamic displacement of the body in liquid (*14*, *15*, *27*–*30*). This "fluid dynamics" hypothesis has several variants (*27*, *30*) but essentially proposes that the straight tail posture during gliding phases reduces drag force and hence saves energy. Here, we propose another, nonexclusive,

[1]Biorobotics Laboratory (BIOROB), École polytechnique fédérale de Lausanne (EPFL), Lausanne 1015, Switzerland. [2]Institute for Systems and Robotics, Instituto Superior Técnico, 1049-001 Lisbon, Portugal. [3]Department of Neurobiology, Duke School of Medicine, Durham, NC 27710, USA.
*Corresponding author. Email: liuxx416@gmail.com (X.L.); auke.ijspeert@epfl.ch (A.J.I.)

hypothesis, which we call an "actuator efficiency" hypothesis: Bout-and-glide swimming enhances energy transfer from electricity (or chemical energy in fishes) to kinematic tail movement. In other words, intermittent swimming allows fish to use their muscles in more energy-efficient regimes than continuous swimming. Although the notion that muscles (and electric motors) have nonlinear efficiencies in terms of payload and contraction velocities is well established (*31*, *32*), here, we explicitly formulated and tested this actuator efficiency hypothesis for intermittent swimming, a context in which it has not previously been examined.

This study, therefore, presents the development of ZBot, inspired by zebrafish larvae. In terms of mechanisms, we present ideas to address design challenges encountered in fishlike robots. We developed a neural model for bout-and-glide swimming, informed by kinematic recordings of larval zebrafish locomotion (*11*). Beyond qualitatively replicating bout-and-glide swimming, this model generates diverse bout-and-glide gaits that closely resemble those observed in live larval zebrafish (*11*). This outcome establishes a foundation for using the model in further investigations of larval zebrafish movement behavior. For example, in a parallel study (*26*), we adapted and integrated this bout-and-glide neural model into a complete sensorimotor neural circuit, enabling the use of simulations and robotic experiments to study the building blocks of visuomotor behaviors. To investigate why aquatic animals exhibit bout-and-glide swimming over a wide range of body sizes, we leveraged the *Re* number, which is proportional to body length (BL) and inversely proportional to liquid viscosity. Instead of changing the robot's size, we adjusted the viscosity of the surrounding liquid. Thus, we evaluated ZBot's dynamic swimming behavior across three conditions: (i) water, (ii) a moderately viscous liquid, and (iii) a highly viscous liquid. Testing swimming in liquids of different viscosities, we show that increasing the liquid viscosity rapidly decreases the traveled distance, whereas it has much less effect on the turning angles. By conducting robotic experiments, we established the connections between swimming variables (tail-beating frequency, tail-beating amplitude, bout frequency, and bout duration) and the resulting behaviors (swimming velocity and turning angle) while swimming in liquids with various viscosities. Last, we demonstrate that intermittent swimming leads to a lower cost of transport (CoT) than continuous swimming, across most of its achievable velocity range, in water and viscous liquids. Our results suggest that the actuator efficiency hypothesis is valid for all swimming regimes that we investigated (both viscous fluids and water), whereas the fluid dynamics hypothesis was only confirmed for swimming in water (high–*Re* number swimming). The energy efficiency advantage arises because intermittent locomotion allows the robot's actuators to operate within a regime of higher inherent efficiency.

RESULTS

ZBot, a robot inspired by zebrafish larvae

ZBot is a robot that closely mimics key morphological features (shape, center of mass, and segmental structure) of zebrafish larvae. The larva was preferred to the adult zebrafish because many insights about behaviors and neural circuits are derived from larval zebrafish due to advantages including optical transparency, rapid generation cycle, easy manipulation, permeability to small molecules, and cost-effectiveness (*33*). In the current study, we used ZBot to investigate swimming behavior. In our parallel investigations, we also used it to study other larval zebrafish behaviors, such as visuomotor processing (*26*) and the vestibular system, thereby reducing the additional costs associated with redeveloping the robotic platform.

To test hypotheses in robotics, it is essential to develop a robot that sufficiently mimics the sensorimotor properties of the animal. For example, studying visuomotor processing requires equipping the robot with cameras, whereas investigating the vestibular system necessitates the use of an inertial measurement unit. To accommodate these diverse needs, the robot should provide high flexibility in sensor installation. In addition, it is important for the robot's morphology to closely resemble that of the real zebrafish larvae. Factors such as shape, center of mass, and weight distribution must be considered to ensure a realistic representation. As a scientific tool, the robot should also prioritize maintenance-friendliness, reliability, and easy access to its components for smooth experimentation and data collection.

To achieve a practical and functional design, we scaled the robot's body by a factor of 200 (see Supplementary Methods), resulting in an approximate length of 80 cm compared with the typical 4-mm length of a zebrafish larva (Fig. 1, A and B, Movie 1). This scaled size was chosen because it enables two key advantages: It accommodates powerful actuators, provides ample internal space for integrating sensors and a relatively heavy lithium polymer (LiPo) battery, and prioritizes easy maintenance to allow researchers to access and adjust the robot's components as needed (fig. S1). ZBot's morphology closely mirrors that of a larval zebrafish, comprising a head segment (housing all essential electronics) and six tail segments actuated by servomotors (Fig. 1C and fig. S2). Inside the head segment, we implemented a three-layer sandwich configuration to organize the required electronics (Fig. 1D), including the central controller, onboard camera, battery, power hub, remote control receiver, and wattmeter (fig. S3), and this layout was designed for easy access and maintenance to enable researchers to install new modules in future studies. Through a remote controller, operators can adjust ZBot's direction, speed, and swimming mode (Fig. 1, E and F), and an onboard first-person-view (FPV) camera transmits real-time video that operators can view using goggles to inspect the environment (Fig. 1, E to G, and movie S1). Beyond supporting remote control and environmental monitoring, this FPV subsystem also offers researchers an opportunity to experience the embodied sensation of swimming like a fish. We also developed a software program that runs on an embedded controller, specifically designed to execute the neural model introduced in subsequent sections, and this program uses multiple threads to enable faster processing and adaptability to various research tasks (fig. S4).

Neural model underlying bout-and-glide swimming

Integrating insights from previous behavioral and modeling studies (*4*, *11*, *34*–*36*), we introduce a computational neural model that can accomplish bout-and-glide swimming (Fig. 2A). This model comprises six types of components: CPGs, a leaky integrator, a behavior determinator, a bout gate, ventral spinal projecting neurons (vSPNs), and motor neurons. The CPGs generate rhythmic tail undulations, which are crucial for swimming propulsion (*4*, *36*). To regulate the activation of CPG outputs, we introduce a leaky integrator and bout gate mechanism. The leaky integrator accumulates descending inputs from visual areas and triggers the bout gate to activate the CPGs when it reaches a preset threshold. In real larval zebrafish, the descending input of swimming is observed in visually responsive neurons of the nucleus of the medial longitudinal fasciculus (*37*).

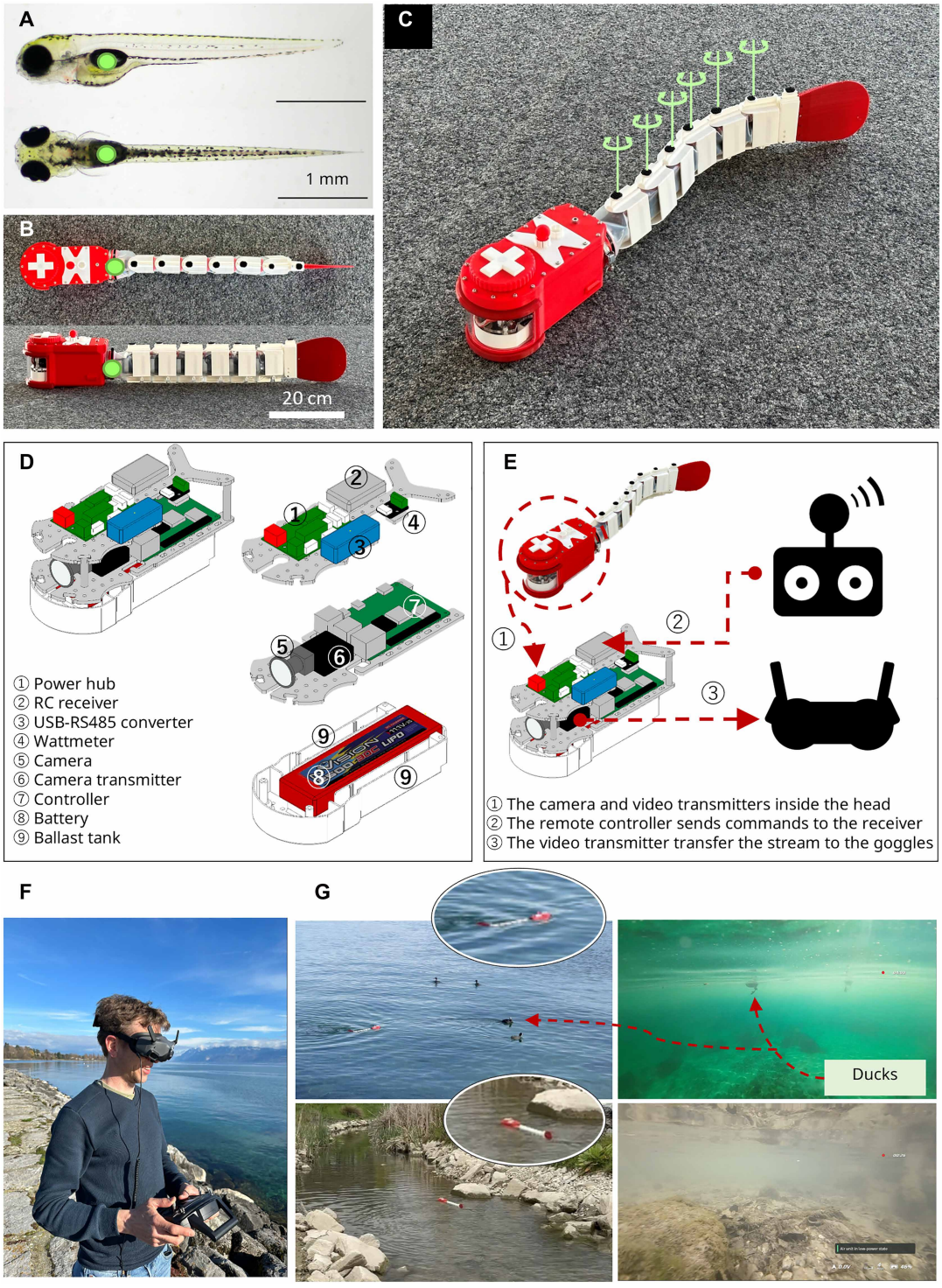

Fig. 1. Overview and design features of ZBot. (**A**) Side and top views of a 5-day-old zebrafish larva. Green dot indicates the position of the center of mass. (**B**) Top and side views of the ZBot. (**C**) Isometric view of the ZBot. Highlighted in green are the six serially linked segments forming six degrees of freedom. (**D**) ZBot contains a three-floor electronic module inside the head module, allowing easy substitution of different electrical components. (**E**) ZBot's remote control operates through an FPV system, allowing users to send commands, such as bout direction, via a remote controller to the robot's onboard receiver. For an immersive experience, users wear FPV goggles that display a live video feed from the onboard camera. (**F**) A user remotely controlling ZBot through this system. (**G**) Additional images showcase ZBot swimming in Lake Léman and the Bief River (Vaud, Switzerland), including a third-person perspective and the live feed captured by the onboard camera.

PHOTO CREDIT: (A) G. VALENTIN/CENTER OF PHENOGENOMICS—EPFL FISH FACILITY

Movie 1. Summary of study. Understanding the neural mechanism and energy efficiency of intermittent swimming via a larval zebrafish–inspired robot (ZBot).

The bout gate controls the amplitude of CPG outputs, exhibiting a fast rise and slow decay pattern [Fig. 2B and fig. S5, in which fig. S5 is adapted from Marques *et al.* (*11*)]. In addition, vSPNs play a key role in directional tail bending during turn bouts (*35*). By specifically modulating the vSPN outputs (Fig. 2C), the model performs either forward (inactive vSPNs) or turning bouts (unilateral active vSPNs, with a fast rise and slow decay pattern; Fig. 2, D and E). To generate the fast rise and slow decay pattern for both bout gate and vSPNs, we used low-pass–filtered exponential functions (Fig. 2, B and C). Motor neurons convert neural signals to physical tail movement, transmitting commands (desired joint angles) to the servomotors. Together, these components form a neural framework for studying and replicating the bout-and-glide swimming behavior observed in larval zebrafish. We present the details of the neural model in the Supplementary Materials and an example of the recorded internal states in data file S1. In this study, we focus on the neural model

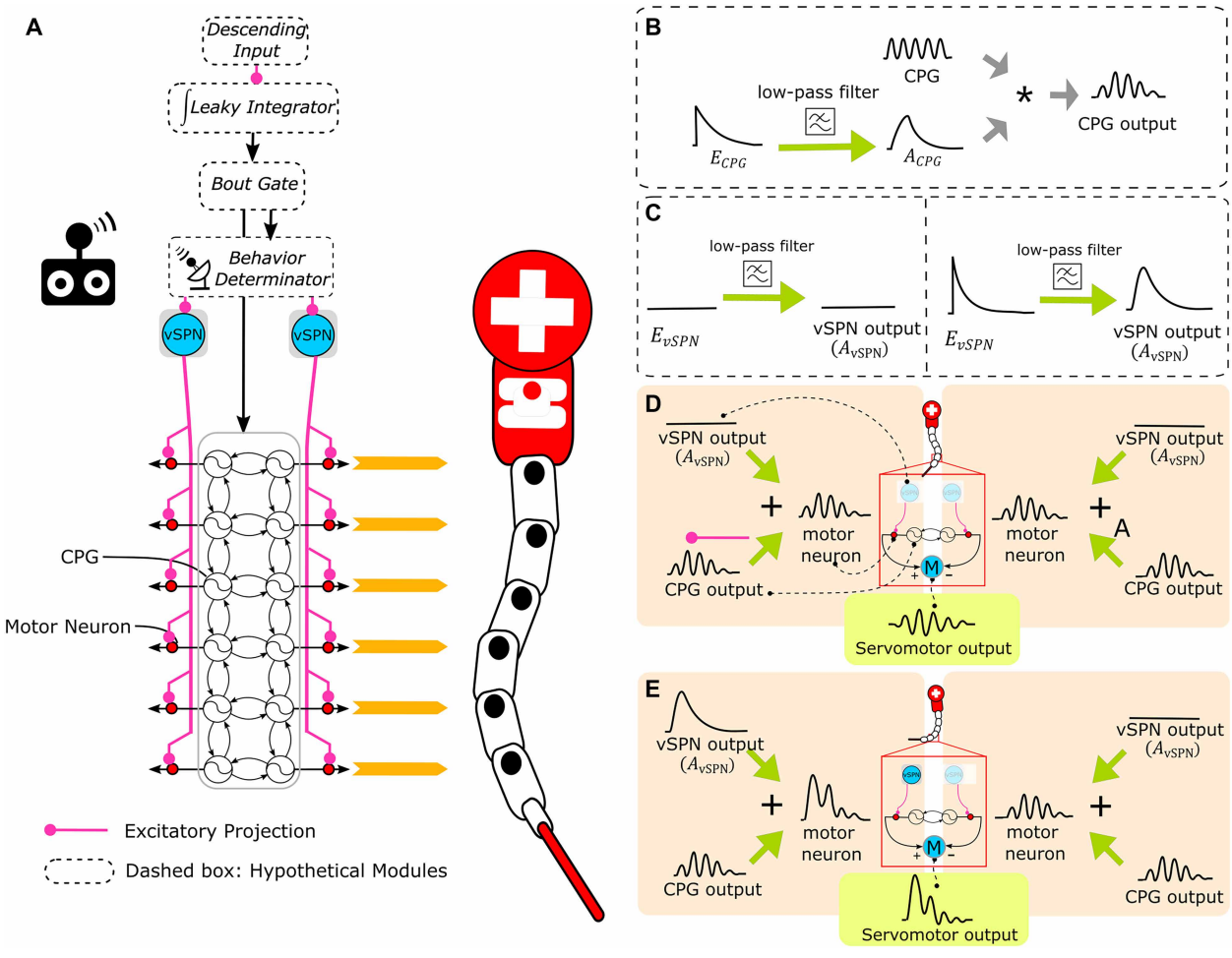

Fig. 2. Neural model underlying bout-and-glide swimming. (**A**) The leaky integrator receives and accumulates descending inputs. The bout gate opens and initializes a bout when the leaky integrator reaches a preset threshold. The behavior determinator selects a behavior from forward, leftward turning, and rightward turning bouts. In the robot, an operator remotely controls the behavioral selection. The vSPNs contribute to the tail bias. In the spinal cord, the CPGs generate the rhythmic signals. The motor neurons integrate inputs from the CPGs and vSPNs. The difference in outputs between left and right motor neurons controls the servomotors in the robot. (**B**) To generate the periodic tail beating, the bout gate opens the CPG. The amplitude of the CPG output is defined by the output of an exponential function through a low-pass filter. (**C**) Deactivated vSPN neuronal output and active vSPN neuronal output. (**D**) To generate a forward bout, the vSPN neurons on both sides of the body remain deactivated. The motor neurons integrate the outputs from the CPG and vSPN on each side of the body. The servomotor output was calculated by taking the difference between the left and right motor neurons. (**E**) The generation of a turning bout is similar to the generation of the forward bout, except that the vSPN on one side of the body generates an active output.

responsible for generating bout-and-glide swimming. In a parallel study from our group (*26*), we adapted and integrated this neural model into a whole neural network for the optomotor response, a visuomotor behavior assay used to investigate vision and brain function. In that study, our emphasis was on visually guided behaviors and the brain's visuomotor neural circuits.

Reproduction of larval zebrafish–like bout-and-glide swimming

We demonstrate that the neural model, when embodied in the ZBot, can produce bout-and-glide swimming behavior that closely resembles that of the real animal (Fig. 3, fig. S5, and movies S2 and S3). We first conducted the swimming experiments in stationary water, a harbor on Lake Léman (Vaud, Switzerland) (Fig. 3A). Compared with a small pool, the wide-open water allowed the ZBot to perform several bouts in sequence and minimized the influence of wave interference, which could arise from the reflection of waves off a pool's walls, potentially affecting the ZBot's swimming behavior. Figure 3B shows recorded frames of a forward bout, a leftward turning bout, and a rightward turning bout from the top view of a hovering camera drone. During the experiments, we set the tail-beating frequency (f_{TB}) to 1 Hz, the ratio of tail-beating amplitude to 1.0, the bout frequency (f_B) to 0.1 Hz, and the bout duration (T_B) to ~5 s, using these parameters as the default setting. We qualitatively confirmed that these parameters could generate larval zebrafish–like swimming behavior (Fig. 3, C and D). The results of head direction and tail-segment angle (Fig. 3C) exhibit similar properties compared with kinematic recordings of larval zebrafish (Fig. 3D and fig. S5, C and

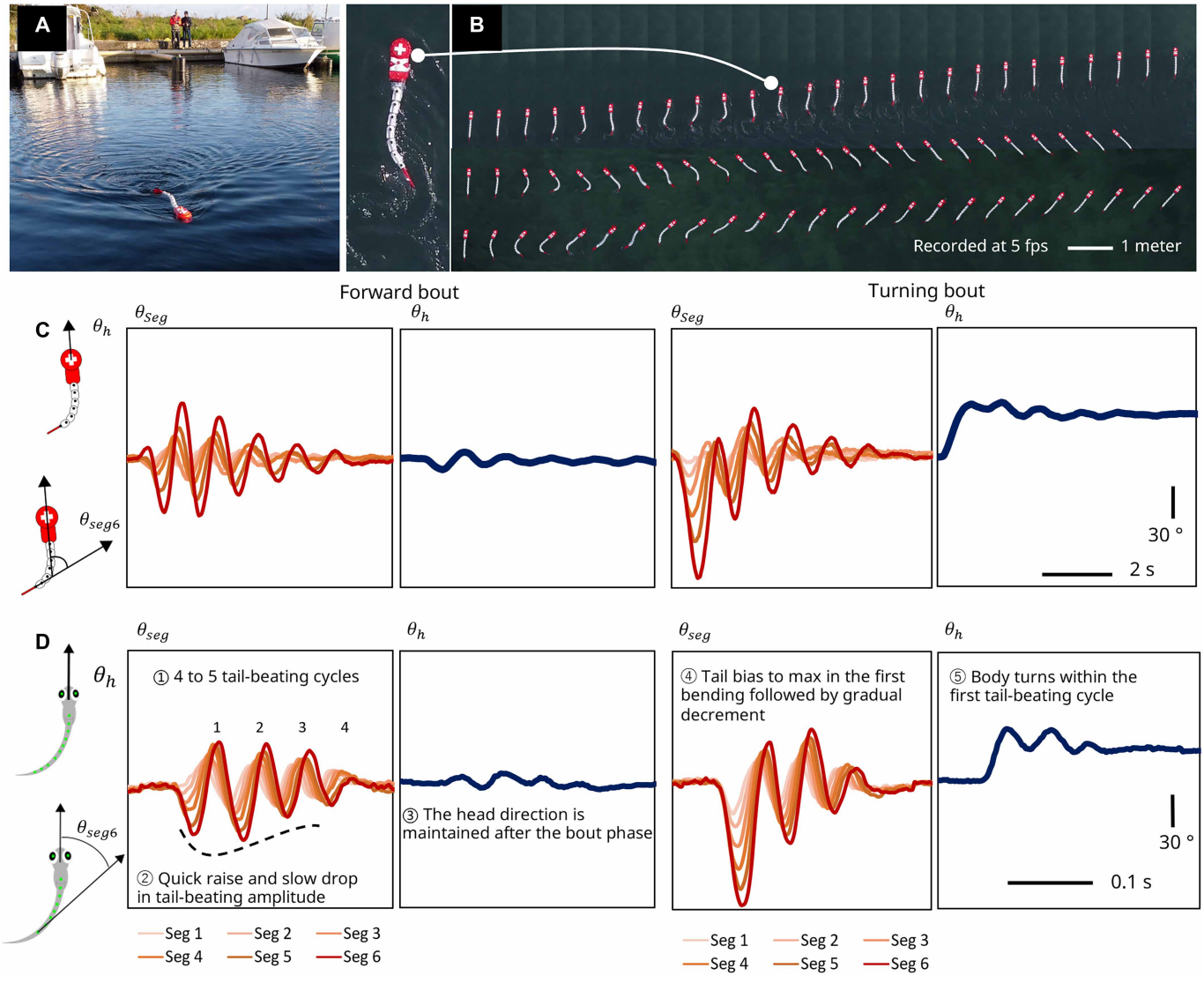

Fig. 3. Robotic bout-and-glide swimming driven by the neural model. (**A**) In the experiments, the robot swam in the harbor of Lake Léman (Vaud, Switzerland) under remote control, such as swimming direction. (**B**) Frames of forward, leftward turning, and rightward turning bouts from a drone view. (**C**) Recorded head direction θ_h and accumulative segmental angles θ_{seg} of a forward bout and rightward turning bout. The recorded data are presented in data file S2. With the embodiment of the neural mechanism, the robot demonstrated kinematic behavior of bout-and-glide swimming similar to that of zebrafish larvae in (D). (**D**) Recorded head direction θ_h and accumulative segmental angles θ_{seg} of a forward bout and rightward turning bout in zebrafish larva swimming.

D). During a forward bout, we observed five tail-beating cycles with a fast rise and slow drop in tail-segment angle amplitude. The head direction remained constant after the bout phase. During a turn bout, ZBot's tail was maximally biased in the turn direction in the first tail-beating cycle, completing the directional change within the first tail-beating cycle, similar to real larval zebrafish (*11*). The bars representing the temporal scale differ between the robot and the zebrafish larva. Despite the similarity mentioned above, there is a notable difference in bout-and-glide distance: Z-Bot's bout-and-glide distance is approximately three times its BL, which is longer than that of zebrafish larvae—their typical bout-and-glide distance ranges from about 0.5 to 1 BL (*11*). In addition, fig. S6 displays the internal state of the neural model in a forward bout, leftward turning bout, and rightward turning bout.

Decreased bout-and-glide distance while swimming in viscous liquid

The ZBot is ~200 times larger than zebrafish larvae, resulting in substantial differences in their respective *Re* numbers during swimming. In water (viscosity = 1 cP), the ZBot operates in a turbulent flow regime, with *Re* values ranging from 6.4×10^4 (during the slowest bout-and-glide swimming) to 1.60×10^5 (during the fastest bout-and-glide swimming). In contrast, zebrafish larvae exhibit bout-and-glide swimming in an intermediate flow regime, with reported *Re* values of 60 to 1400 (*22*). To test the ZBot in lower *Re* number regimes, leveraging the inverse relationship between *Re* number and fluid viscosity, we prepared liquids with moderate (213.9 cP) and high (457.0 cP) viscosities in a small swimming pool. The moderately viscous liquid enables the ZBot to swim under hydrodynamic conditions similar to those of zebrafish larvae. We also tested the ZBot's swimming performance in a highly viscous liquid, because we sought to investigate the robot's dynamic behavior in viscous flow regimes. The increased viscosity led to decreased bout distance, glide distance, bout-and-glide distance, and gliding ratio when swimming in the viscous liquid (Fig. 4, A and B, and movie S4). In the moderately viscous liquid, the ZBot achieved average swimming velocities from 0.01 to 0.12 m/s (about 0.01 to 0.15 BL/s, shown in Fig. 5D), corresponding to *Re* values of 37.4 to 448.8, which aligns with the *Re* number range of zebrafish larvae. Under default swimming parameter settings, the ZBot's bout-and-glide distance in this moderately viscous liquid was ~0.74 m (or 0.92 BL)—slightly shorter than its BL, matching the forward bout-and-glide distance observed in zebrafish larvae (*11*), which is about 0.5 to 1 BL. In the highly viscous liquid, the ZBot's bout-and-glide swimming yielded average velocities from near zero to 0.05 m/s (near 0 to 0.06 BL/s), resulting in *Re* values of 1 to 87.5, which fall close to the viscous flow regime (*38*). In this highly viscous liquid, the ZBot exhibited near-zero gliding after each forward bout. Compared with the marked influence on the traveled distance, the influence on the turning angle of different viscosities was much smaller. For example, with the default parameter settings, the ZBot displayed an average turning angle of 62.6° in water, whereas in highly viscous liquid, the ZBot showed an average turning angle of about 45.5° (Fig. 4, C and D, and movie S4).

Diverse kinematic outputs by manipulating the parameters in the neural model

In addition to typical forward and turning bouts, zebrafish larvae can perform a variety of swimming maneuvers (*11*). Similarly, the neural model, through parameter manipulation, can produce diverse tail-beating patterns (Fig. 6, fig. S7, and movie S5). Figure 6 and fig. S7 demonstrate the desired joint-angle outputs from the robotic controller under various parameter settings. These include the ratio of tail-beating amplitude, tail-beating frequency, bout frequency, bout duration, and tail-beating bias (by modulating E_{vSPN0}, which represents the initial value of the vSPN). Details of the neural model and its parameters are provided in Supplementary Methods. Some of the generated patterns resemble kinematic recordings of zebrafish larvae. For example, varying the ratio of tail-beating amplitudes among values of 0.33, 0.67, and 1 produces kinematic outputs that resemble forward swimming gaits observed in zebrafish larvae: approach swim, slow 1 swim, and slow 2 swim, respectively, as described by Marques *et al.* (*11*). Similarly, tail-beating bias varies with E_{vSPN0}: Ratios of 0.8, 1, and 1.2 yield outputs resembling high-angle turn, routine turn, and spot avoidance turn of zebrafish larvae, respectively (*11*, *39*). Bout frequency can also be modulated by descending input (Fig. 6D).

Linking the bout-and-glide swimming parameters to velocity

Parameters such as tail-beating frequency and amplitude can influence swimming velocity. However, only a few studies have focused on bout-and-glide swimming (*27*). We evaluated the relationship among average swimming velocities, power consumption, and various swimming parameters while swimming in both water and viscous liquids. Figure 5A and fig. S8 show the scenario of the experiments in water and in viscous liquid, respectively. We describe the details of the experimental setting in Materials and Methods.

Specifically, we systematically examined the effects of different parameters, including tail-beating frequency, ratio of tail-beating amplitude, bout frequency, and bout duration, on swimming velocities (Fig. 5B). During tests evaluating the effects of a single parameter, we held the other parameters constant. We also conducted experiments to measure the average velocity of ZBot while swimming in viscous liquids (see Supplementary Methods for the measurements). Figure 5C shows an example of recorded velocity using the default swimming parameter setting while swimming in water. The recorded (instantaneous) velocity demonstrates a rapid rise and gradual decline within each bout cycle. During the bout phase, the velocity exhibits periodicity, likely because of self-motion induced by tail beating along the anterior-posterior axis. Figure 5D presents the velocity as a function of tail-beating frequency, tail-beating amplitude ratio, bout frequency, and bout duration, respectively. We set the ranges for each parameter within the limits of the servomotor power output. The velocity increases with the increment of each parameter. Among these parameters, increasing bout frequency shows a trend toward higher average swimming velocity compared with the other parameters. In all experiments, the increment was less substantial for higher viscosities. This may be attributed to increased drag forces with higher swimming velocities. In addition, excessively high amplitudes result in excessive bending, leading to internal body collisions and a loss of propulsive forces. We did not test the effects of bout frequency under viscous liquid conditions because the swimming pool was too small. The data can be found in data file S4.

Figure S9 displays the average turning angle as a function of the initial value of the exponential function of vSPN (E_{vSPN0}) during bout-and-glide swimming. In the experimental setup, a camera drone hovered midair to capture videos of the robot performing

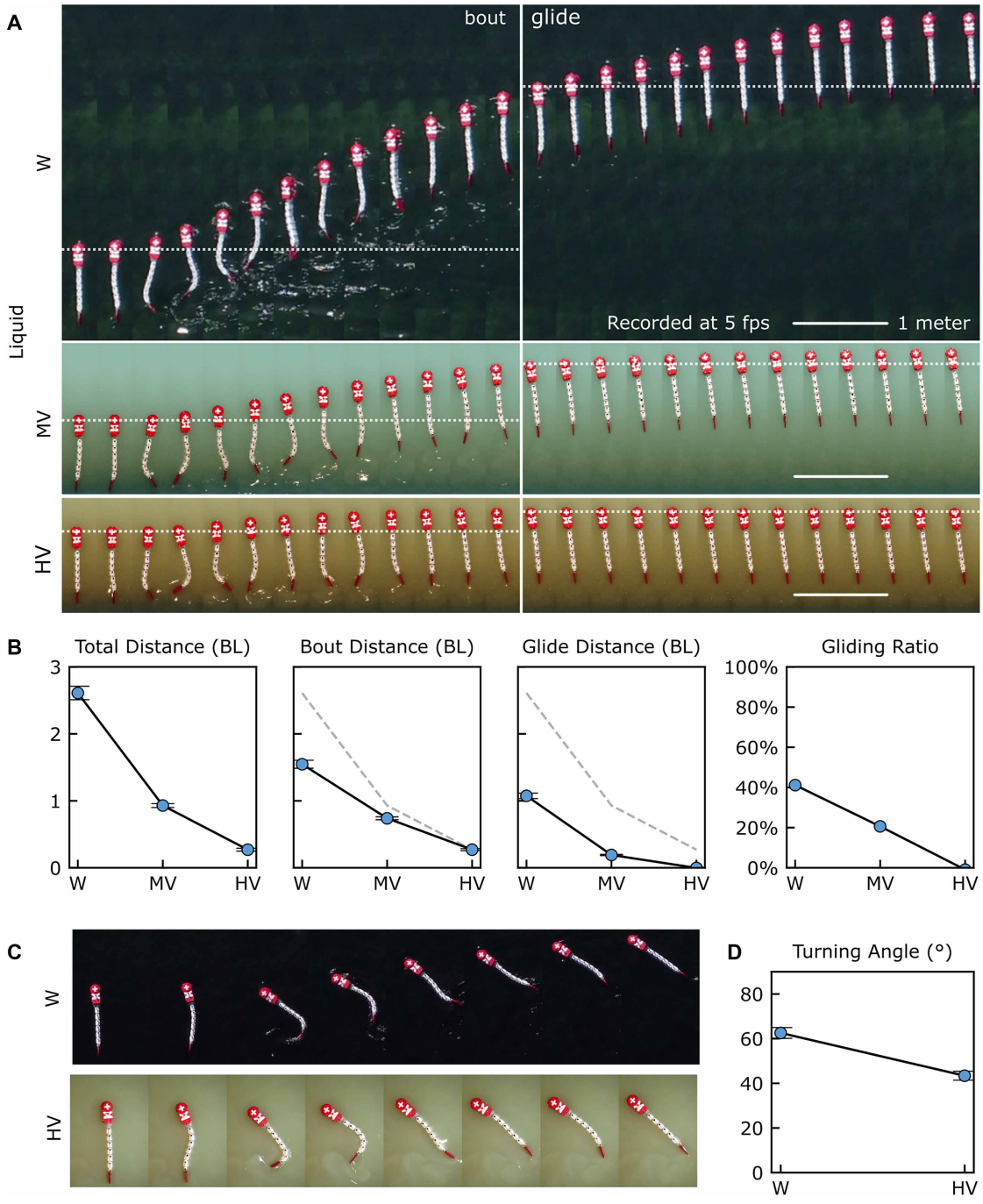

Fig. 4. Increased viscosity drastically reduces bout distance, glide distance, and gliding ratio but minimally affects turning angle. (**A**) Frames of the ZBot performing bout-and-glide swimming in water (W, 1 cP), moderately viscous liquid (MV, 213.9 cP), and highly viscous liquid (HV, 457.0 cP), enabling swimming in the turbulent flow regime, intermediate flow regime, and viscous flow regime, respectively. Dashed lines mark the starting position of each bout or glide. (**B**) Increased viscosity drastically reduces bout distance, glide distance, and gliding ratio. Each data point has a sample size of three. (**C**) Frames of the ZBot executing turning bouts in water and highly viscous liquid. (**D**) The effect of viscosity on turning angle is substantially smaller than its effect on the distance in (B). We collected 13 and 6 samples for the turning bouts in water and highly viscous liquid, respectively. Movie S4 shows the corresponding videos.

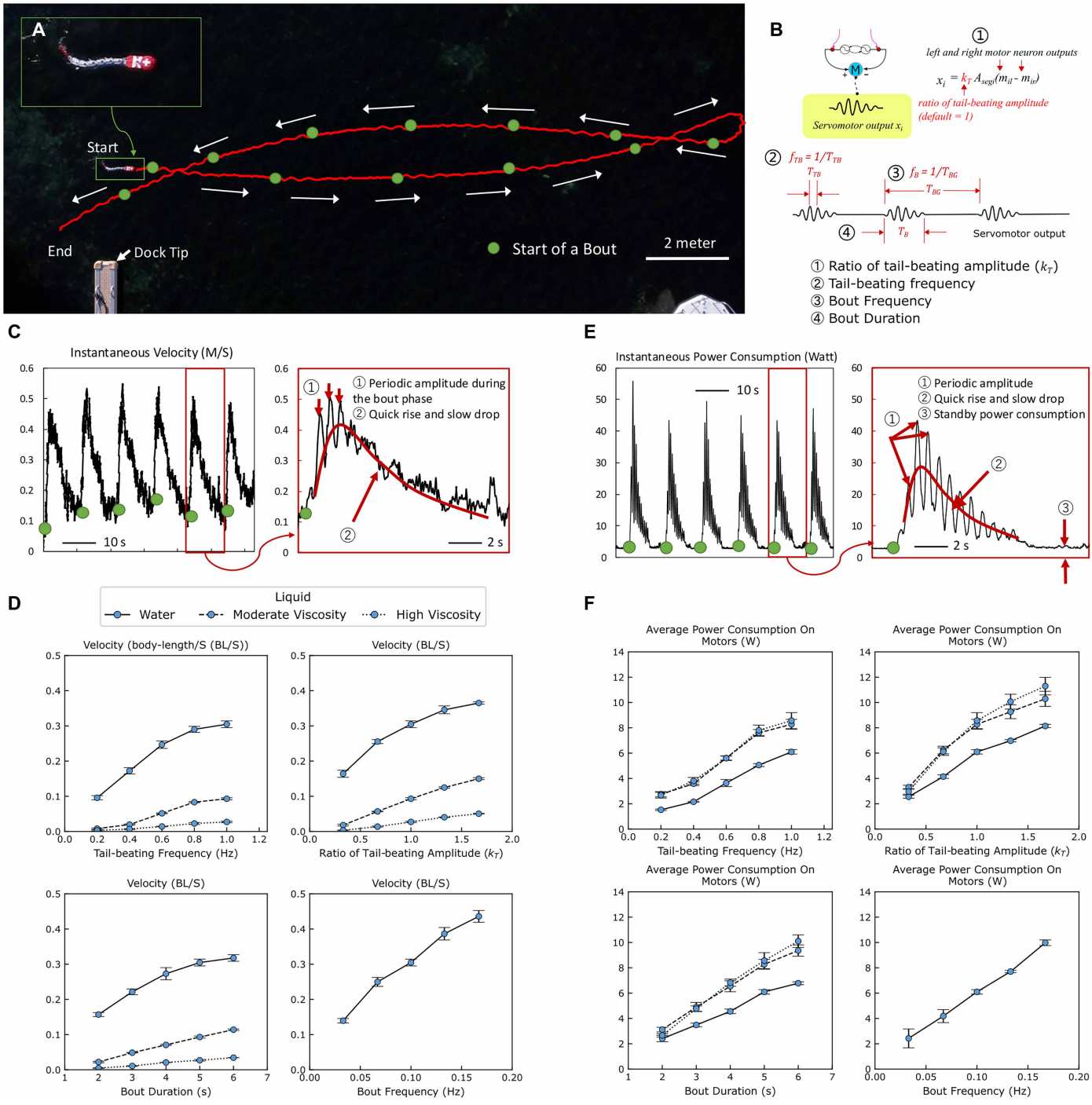

Fig. 5. Robotic experiments relate average swimming velocity and power consumption to key swimming parameters in bout-and-glide swimming. (**A**) Experimental setup for water-based trials: A camera drone hovers overhead to record ZBot swimming; under remote control, the robot traverses from left to right across the camera view and returns left, with its trajectory marked by a red line and bout start positions indicated by green dots. (**B**) Definition of swimming parameters: tail-beating frequency, tail-beating amplitude ratio, bout frequency, and bout duration. (**C**) Example of recorded velocity during six forward bouts (default parameters and water). A zoomed view reveals periodic velocity oscillations during the bout phase, characterized by a rapid rise and gradual decline in velocity, mirroring the trend of tail-beating amplitude (see Fig. 3C). (**D**) Average swimming velocity analyzed as a function of the four swimming parameters: Velocity increases with higher values of each parameter, although the rate of increase diminishes; average velocity also rapidly decreases with rising liquid viscosity. (**E**) Example of recorded power consumption during six bouts (water). A zoomed view shows periodic power oscillations during the bout phase, following a trend similar to tail-beating amplitude. (**F**) Average power consumption analyzed as a function of the four swimming parameters: Power consumption increases with higher values of each parameter, and rising viscosity leads to a slight increase in power consumption. Vertical bars in (D) and (F) represent SD; raw recorded data are provided in data files S4 and S5. Each data point has a sample size of 6 to 17.

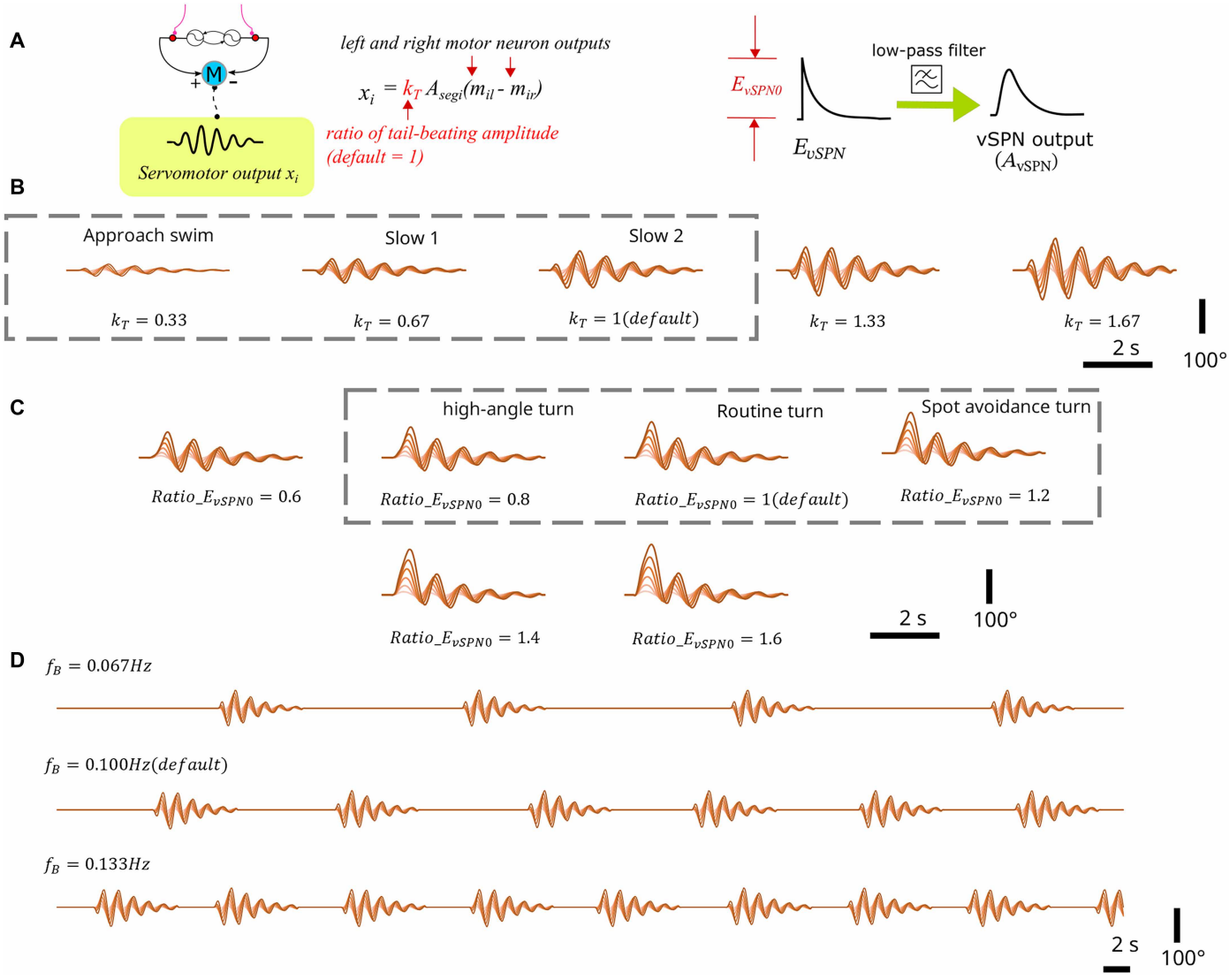

Fig. 6. Diverse kinematic output from the robotic controller by manipulating neural model parameters. (**A**) Swimming parameters include the ratio of tail-beating amplitude (k_T) and initial value of vSPN (E_{vSPN0}). The former determines the tail-beating amplitude, and the latter determines the bias of the tail in turning bouts. (**B**) Kinematic output driven by different ratios of k_T: Ratios of 0.33, 0.67, and 1 produce kinematic outputs resembling approach swim, slow 1 swim, and slow 2 swim of zebrafish larvae, respectively (*11*). (**C**) Kinematic output driven by different ratios of E_{vSPN0} (influencing the tail bias): Ratios of 0.8, 1, and 1.2 yield outputs intuitively similar to high-angle turn, routine turn, and spot avoidance turn of zebrafish larvae, respectively (*11*). (**D**) Bout frequency can be modulated by the descending input (see Fig. 2A). Example videos driven by the aforementioned kinematic outputs can be seen in movie S5. The detailed kinematic data are presented in data file S3.

leftward turning bouts under remote operation. The trajectories of the robot are marked by a red line, with green points indicating the start of each bout. A total of ~20 bouts were performed per trial. Tail bias was modulated by varying E_{vSPN0} on the ipsilateral side of the turning direction.

Linking the bout-and-glide swimming parameters to power consumption

We recorded the power consumption of the ZBot while systematically varying parameters, including tail-beating frequency, ratio of tail-beating amplitude, bout frequency, and bout duration, for swimming in both water and viscous liquid. Figure 5E displays an example of the recorded power consumption during a forward bout of the ZBot using the default parameter setting in water. Upon closer examination, the power consumption amplitude rises quickly after the initiation of a bout and then gradually decreases. This trend is similar to the tail-beating amplitude shown in Fig. 3C and instantaneous velocity shown in Fig. 5C. Power consumption exhibits periodic behavior during a bout because of varying power requirements during the tail-beating cycle. During the gliding phase, a constant standby power consumption of ~3 W was observed, used to power the microcontrollers of the servomotors. Figure 5F shows power consumption to be a function of tail-beating frequency, tail-beating amplitude ratio, bout frequency, and bout duration, respectively. These figures reveal that power consumption increases with higher values of these parameters. The data can be found in data file S5.

Linking the continuous tail-beating swimming parameters to average velocity and power consumption

To compare intermittent and continuous swimming, we modified the neural model by keeping the bout gate constantly open, enabling continuous swimming behavior in the ZBot (see movie S6 and Supplementary Methods). Figure S10A illustrates the experimental scenario, with a camera drone filming the ZBot from above. During the experiments, we systematically varied the tail-beating frequency and amplitude while the robot engaged in continuous swimming (fig. S10B). Under remote operation, the ZBot followed a trajectory from left to right in the camera view and then back to the left, as depicted by the red line. To assess velocity, we recorded the ZBot's position every 5 s, marked by green dots in fig. S10A. Figure S10C presents the measured instantaneous velocity of the ZBot, displaying fluctuations due to differences in the phase of tail beating. In fig. S10D, we show the average swimming velocity as a function of the tail-beating amplitude ratio at different tail-beating frequencies. The results demonstrate an increase in average velocity with higher tail-beating amplitude and frequency. However, the rate of increment decreases as these parameters continue to increase. This trend is similar to what we observed in bout-and-glide swimming in Fig. 5D. In addition, fig. S10E displays the measured instantaneous power consumption, again showing fluctuations related to the phase differences in tail beating. Last, fig. S10F presents the average power consumption as a function of the ratio of tail-beating amplitude and tail-beating frequency. The increment of either the tail-beating amplitude or the frequency increases the average power consumption. The detailed data can be found in data files S6 and S7.

Bout-and-glide swimming delivers better energy efficiency at its achievable velocity range

Using the datasets on-average velocity and power consumption presented in Fig. 5 and fig. S10, we calculated the CoT and plotted CoT against swimming velocity for both bout-and-glide swimming and continuous swimming (Fig. 7A; see Supplementary Methods for calculation details). To generate fitted curves for each swimming mode, we first identified minimum CoT points using a convex hull algorithm and then fit a quadratic polynomial via least squares regression to capture the velocity-CoT relationship (see Materials and Methods for details). Fitted curves for both swimming modes reveal U-shaped CoT curves, each consisting of two phases: a decrement phase (CoT decreases as velocity increases) and an increment phase (CoT increases as velocity continues to rise). For bout-and-glide swimming, the velocity corresponding to minimum CoT occurs at ~0.18 BL/s; in contrast, the velocity corresponding to minimum CoT for continuous tail beating occurs at ~0.3 BL/s. At all reachable velocities for bout-and-glide swimming (<0.32 BL/s), the ZBot exhibited lower CoT during bout-and-glide locomotion compared with continuous tail beating, even when achieving similar swimming velocities. However, the limited duty cycle of tail beats in bout-and-glide mode prevents the robot from reaching high velocities (>0.32 BL/s) with this locomotion strategy. While swimming in viscous liquids, the ZBot exhibited a monotonically decreasing CoT, a distinct departure from the U-shaped CoT curves observed in water. Even with this altered CoT profile, the ZBot still achieved lower CoT when using bout-and-glide swimming compared with continuous tail beating, as shown in Fig. 7 (B and C).

Bout-and-glide swimming improves actuator operating efficiency

In fishlike swimming, two critical phases of energy transfer govern efficiency: For our robot, these include the conversion of electrical power to the kinematic motion of tail segments and the conversion of this kinematic motion to dynamic body displacement. The first phase is primarily dictated by actuator efficiency. For contextual clarity, we plotted energetic efficiency as a function of the ratio relative to maximum payload for two systems: the Dynamixel XM430-W210-R servomotor [used in our experiments, with data from the manufacturer's database (*31*) shown in Fig. 7D(i)] and mouse soleus and extensor digitorum longus (EDL) muscles [as reported by Smith *et al.* (*32*); Fig. 7E]. For the servomotor data, the horizontal axis represents the ratio relative to maximum torque [estimated at 2 Nm (dynamic torque) from the datasheet (*31*)]. The torque has a near-linear relationship to the power input. The efficiency of the servomotors shows a similar trend compared with the biological muscles, because both actuators exhibit high energetic efficiency in the mid-range of the payload regime. In contrast, efficiency decreases at both low and high payload ranges for both actuators.

As discussed in the Introduction, so far, the energy efficiency of intermittent swimming has been attributed mainly to a fluid dynamics hypothesis, namely, the proposition that the straight-tail posture during gliding phases reduces drag force (*14*, *15*, *28*–*30*). Here, we proposed and tested an alternative actuator efficiency hypothesis, namely, that intermittent swimming allows fish and robots to use their actuators in more energy-efficient regimes than continuous swimming. To verify whether bout-and-glide swimming reduces CoT by improving actuator efficiency, we analyzed the electrical power input of servomotors and selected representative data points for each swimming mode, corresponding to low, moderate, and high average swimming velocities. We also estimated servomotor energy efficiency during swimming by combining recorded electrical power consumption with the manufacturer-provided payload-efficiency relationship. Increasing ZBot's average swimming velocity was associated with higher servomotor payload—an example of this is servomotor 5 (the fifth motor from the head) shown in (ii) and (iii) of Fig. 7D. We selected this motor because it exhibits a wide range of power inputs (from low to high), making it representative of actuator behavior across different conditions. Figure 7F displays the recorded power input and estimated energy efficiency of servomotor 5 over a 5-s swimming interval for both bout-and-glide and continuous tail-beating swimming. The servomotor's power input shows an oscillatory pattern, with a minimum value near zero, and this oscillation in power input generates a corresponding oscillatory pattern in energy efficiency. For both swimming modes, increasing swimming velocity (typically driven by a larger tail-beating amplitude and higher tail-beating frequency) was associated with higher energy efficiency. Figure 7G compares the average energy efficiency of the selected data points for both swimming modes, confirming that higher velocity improved the overall energy efficiency of servomotor 5 in our experiments. Last, we compared the overall energy efficiency of all servomotors between bout-and-glide and continuous tail-beating swimming at matched average velocities (shown in Fig. 7H). This analysis reveals that, at similar average velocities, servomotors exhibit higher energy efficiency during bout-and-glide swimming than during continuous tail beating.

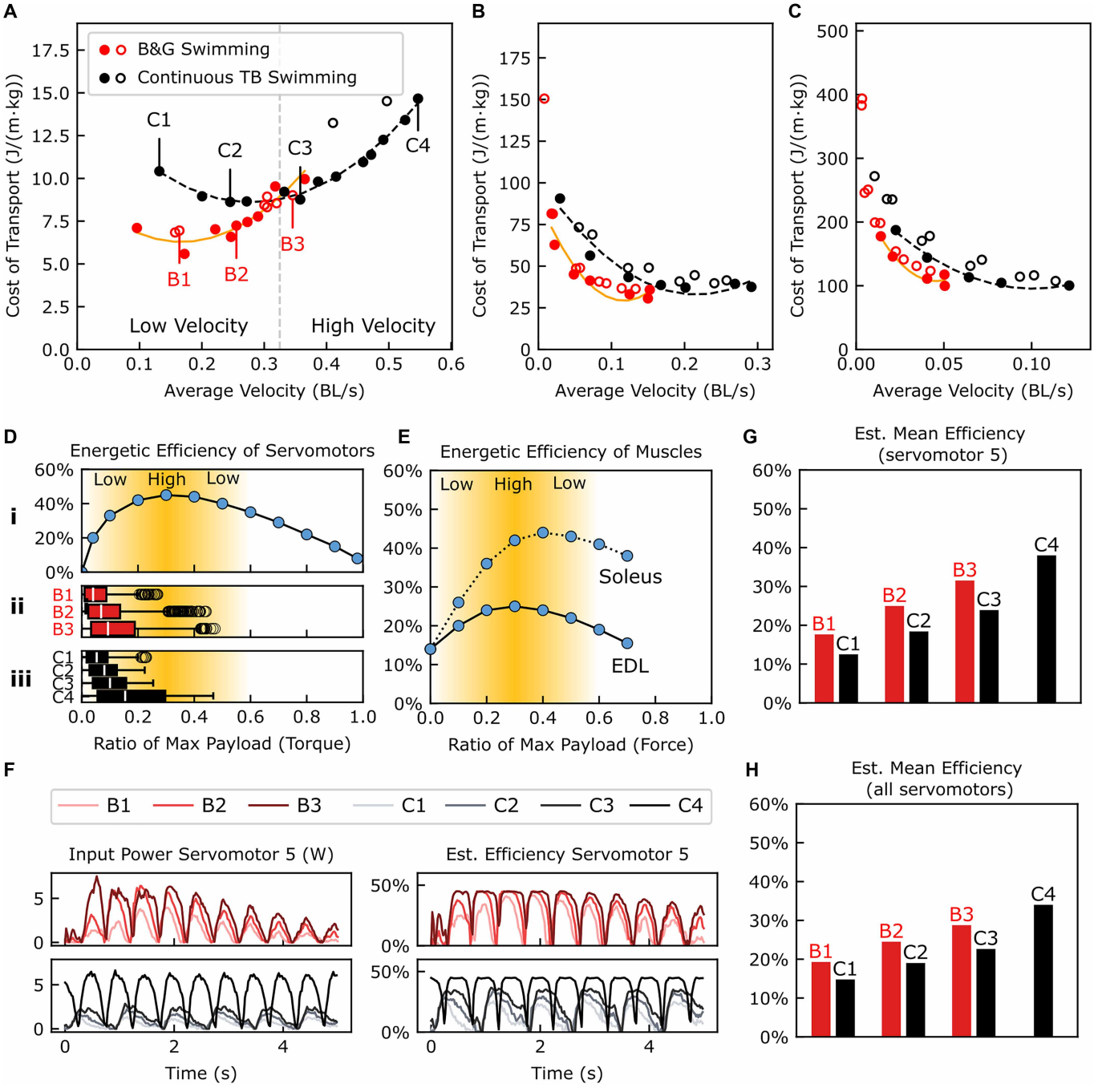

Fig. 7. Bout-and-glide swimming enhances energetic efficiency in the ZBot. (**A**) Robotic CoT across different swimming velocities for bout-and-glide (B&G) swimming and continuous tail beating in water; fitted curves for both modes exhibit a U shape (only filled data points were used to generate lines), with bout-and-glide swimming yielding lower CoT than continuous tail beating across most of its achievable velocity range (B1, B2, and B3 = selected bout-and-glide data points at low/moderate/high velocities; C1, C2, C3, and C4 = selected continuous tail-beating data points at low-to-high velocities). (**B** and **C**) Robotic CoT across different swimming velocities for bout-and-glide swimming and continuous tail beating in moderate and high viscous liquid swimming. The fitted curves demonstrate a monotonic decrease with higher average velocity. (**D**) (i) Energetic efficiency of the ZBot's servomotor; (ii and iii) payload distribution of tail servomotor 5 corresponding to the selected data points in (A); ratio = 1 indicates a payload of 2.0 Nm. (**E**) Energetic efficiency of biological soleus and EDL muscles where both servomotors and biological muscles exhibit higher efficiency in the midrange of their payload regimes (raw data in data file S8). (**F**) Recorded electrical input power and estimated efficiency of servomotor 5 during swimming, showing an oscillatory pattern with power and efficiency minima near zero. (**G**) Estimated efficiency of servomotor 5, which increased with rising swimming velocity. (**H**) Estimated average efficiency of all tail servomotors, which increased with rising swimming velocity. At matched average velocities, bout-and-glide swimming enhanced the average efficiency of the ZBot's servomotors relative to continuous tail beating. Recorded data are provided in data files S8 to S10.

Energy efficiency during swimming in intermediate flow regime and viscous flow regime

Zebrafish larvae operate in intermediate–*Re* number regimes. To investigate how hydrodynamic conditions affect energy efficiency across swimming modes, we compared the energy consumption of intermittent versus continuous swimming in the moderately viscous (213.9 cP) and highly viscous (457.0 cP) liquids. Figure 7 (B and C) shows the velocity-CoT relationships for these conditions, with fitted curves characterizing the patterns. Unlike in water, in viscous liquids across the tested velocities, the CoT fitted curves for both swimming modes decrease monotonically with increasing average velocity. This divergence likely arises from differences in drag force scaling: In intermediate and viscous flow regimes, drag is proportional to velocity (rather than velocity squared, as in turbulent water flow), slowing the rate of drag increase.

Servomotor internal states—including power input and estimated efficiency trends—remained consistent with those observed in water. Increasing velocity elevated motor payload, as shown by torque outputs from servomotor 5 [(ii) and (iii) of figs. S11B and S12B]. Input power and estimated efficiency of servomotor 5 during swimming in moderately and highly viscous liquids are displayed in figs. S11C and S12C, respectively. Figures S11D and S12D show that servomotor efficiency rises with swimming velocity, with figs. S11E and S12E further demonstrating that higher velocities enhance overall efficiency across all servomotors. Critically, across both viscous liquids, ZBot achieved higher energy efficiency during bout-and-glide swimming than during continuous tail-beating swimming at matched velocities (figs. S11F and S12F). Given that gliding distance shortens rapidly with increasing viscosity (and decreasing *Re* number), as shown in Fig. 4, the improved energy efficiency during swimming in viscous liquid can mainly be attributed to bout-and-glide swimming enhancing actuator efficiency, such as our actuator efficiency hypothesis, as demonstrated in figs. S11F and S12F. The fluid dynamics hypothesis contributes to efficiency gains in water but can hardly explain efficiency gains in highly viscous fluids, because gliding distance is near zero and thus cannot contribute meaningful drag reduction.

DISCUSSION

In this work, we developed a larval zebrafish–inspired robot, ZBot, to systematically test neural control models and their effects on locomotion. Despite size differences between ZBot and larval zebrafish, the robot successfully replicated larval zebrafish–like bout-and-glide swimming, relying on the bout-and-glide neural model proposed in this study. The viscosity of liquid markedly shortened the traveled distance of bout-and-glide swimming while minimally influencing the turning angle. We evaluated how various parameters—including tail-beating frequency, tail-beating amplitude, bout frequency, and bout duration—affected both swimming velocity and power consumption. In addition, we investigated and compared the CoT during bout-and-glide swimming versus continuous swimming. The findings show that bout-and-glide swimming outperformed continuous tail-beating swimming in terms of energetic efficiency across its achievable velocities (below 0.32 BL/s for our robot), because intermittent locomotion constrains the robot's actuators to operate within a regime of higher inherent efficiency. However, because of the limited duty cycle of tail beating in bout-and-glide swimming, the robot could not achieve high swimming velocities (above 0.32 BL/s for our robot) using this locomotion mode.

Aquatic animals, including zebrafish larvae, exhibit various swimming gaits, such as forward bouts with different velocities and distances as well as turning bouts (*11*, *37*). A fundamental question arises regarding the mechanisms underlying the generation of these diverse gaits. Our abstract neural model in Fig. 2 demonstrates the capability to generate both forward bouts and turning bouts (Fig. 3), and by modifying the parameters, the model allows the robot to exhibit bouts with different swimming velocities (Fig. 5). Our model provides a potential explanation of gait generation from an engineering perspective. Our study also demonstrates that the neural model for bout-and-glide swimming can be compared with the CPG model that can generate continuous tail-beating swimming. The main difference is that the model for bout-and-glide swimming requires an additional bout gate to regulate the time-varying amplitude of CPG output. In the zebrafish larvae, the generation of different gaits may involve distinct neuron types and circuits, recruiting different motor neurons in the spinal cord (*4*). For instance, routine turning with smaller turning angles involves vSPNs (*35*), whereas escapes with larger turning angles require Mauthner neurons (*40*, *41*). Also, it is known that different CPG subcircuits are activated for different speeds in adult zebrafish (*42*).

Beyond qualitatively generating bout-and-glide swimming, our model demonstrates the ability to produce diverse kinematic outputs through parameter manipulation (Fig. 6 and fig. S7). Some of these outputs resemble kinematic recordings of specific gaits observed in the bout-and-glide swimming of zebrafish larvae (*11*). In addition, the model can generate bouts with a wide range of frequencies by modulating the descending input (Fig. 6D and fig. S7E). This capability not only provides insights into the underlying neural mechanisms from an engineering perspective but also makes the robot a valuable tool for investigating various intelligent behaviors of zebrafish larvae. Zebrafish larvae exhibit different swimming behaviors, such as forward or turning bouts, and adjust their bout frequency in response to external sensory inputs, such as visual stimuli (*3*). A notable example is the optomotor response, where zebrafish larvae tend to turn and follow ground-based visual stimulation (*5*, *35*). Leveraging the properties of our neural model, we conducted a parallel study to investigate the optomotor behavior of zebrafish larvae (*26*).

We further investigated energetic efficiency using the developed ZBot. Many studies argue that bout-and-glide swimming is more energy efficient than continuous swimming (*14*, *15*, *27*–*30*). Parallel to our work, two recent studies on fishlike robots also demonstrated the energy efficiency benefits of bout-and-glide swimming (*27*, *43*) (in water, without tests in viscous liquids). Our results in Fig. 7A show that the robot achieved better overall energy efficiency with bout-and-glide swimming compared with continuous tail-beating swimming—consistent with findings from robotic experiments and observations in fishes mentioned above. These trends also resemble the CoT patterns seen in animal locomotion, such as fast fish swimming (*44*, *45*) and horse walking or trotting (*46*, *47*).

When considering the energy efficiency of fishlike swimming, two crucial energy transfer processes occur during locomotion: The first is the transfer of chemical energy (in fish) or electrical power (in robotic fish) into kinematic tail beatings; the second is the transfer of kinematic tail beatings into body displacements in water. All previous studies have focused only on the second process, positing that the straight tail posture during the gliding phase helps reduce fluid drag (*15*, *27*, *29*, *43*), which we call the fluid dynamics

hypothesis. In contrast with prior work, we proposed and tested an alternative actuator efficiency hypothesis, namely, that intermittent swimming allows fish and robots to use their actuators in more energy-efficient regimes than continuous swimming. We found that bout-and-glide gaits constrained the robot's actuators to operate within a regime of inherently higher efficiency. This held true for swimming in both water and viscous liquids, as shown in Fig. 7 and figs. S11 and S12. When ZBot swam in viscous liquids, the CoT trend decreased monotonically with increasing velocity for the velocity range that we explored (figs. S11 and S12)—a departure from the U-shaped CoT trend observed in water. This result aligns with monotonically decreasing patterns seen in slow fish swimming (*44*). The difference likely arises from how drag scales with velocity: In water, ZBot swam faster, and drag was proportional to velocity squared, leading to sharp CoT increases at high speeds; in viscous liquids, ZBot swam slower, and drag was approximately proportional to linear velocity.

Although animal experiments, robotic studies, and simulations have all demonstrated that bout-and-glide swimming contributes to energy transfer from kinematic tail movement to dynamic body displacement in turbulent flow regimes (*Re* number > 1000) (*14*, *15*, *28*–*30*), this energy efficiency is typically attributed to the straight tail posture reducing drag during gliding. This mechanism, however, may not hold in viscous flow regimes. Our results in Fig. 4 show that increasing viscosity rapidly shortens the gliding distance; in highly viscous liquids, the gliding distance nearly disappears entirely. This phenomenon has also been observed in zebrafish swimming, where the proportion of distance covered during gliding is only about 10% (*11*). Thus, in viscous flow regimes, such as when our robot swims in viscous liquids or when small organisms like zebrafish larvae swim, the primary contribution of bout-and-glide swimming to energy efficiency lies in optimizing actuators (or biological muscles, in the case of zebrafish) to operate within a higher-efficiency regime. In summary, the fluid dynamics hypothesis is valid in high–*Re* number swimming, whereas our actuator efficiency hypothesis is valid for both high– and low–*Re* number swimming.

Instead of the hill-like relationship, which is analogous to the efficiency-payload (torque) relationship of actuators shown in Fig. 7D(i), the velocity efficiency of the actuators exhibited a monotonic increase across most of the range tested in our study, as depicted in Fig. 7, G and H. It is likely that this efficiency curve would have declined for higher payloads, but we did not investigate higher swimming velocities to avoid large tracking errors (servomotors not being able to precisely follow the commands from the neural model) and risk damaging the motors.

Although we demonstrate that bout-and-glide swimming can enhance energetic efficiency, many aquatic creatures, both as small as the larval zebrafish such as *Danionella* (*24*, *25*) and as large as adult zebrafish and salamanders (*4*, *36*), rely mainly on continuous tail beating for propulsion. Our results suggest that these different swimming preferences might be explained by differences in muscle properties and in their efficiency curves with respect to payload. For instance, adult zebrafish have three distinct muscle fiber types: red, white, and intermediate pink, unlike larval zebrafish, which have mainly the white fiber type (*4*, *48*). The red fibers are aerobic and rich in myoglobin, whereas the white fibers are anaerobic, large-diameter fibers. These specialized properties allow adult zebrafish to perform low-force, sustained movements or powerful, short-duration bursts. In the case of adult zebrafish, selectively recruiting specific muscle fibers may therefore be sufficient to optimize energetic efficiency across the necessary range of swimming velocities and be a good alternative mechanism to switching between intermittent and continuous swimming.

Our robot enables qualitative reflection of energetic efficiency in fish swimming but is limited in its ability to replicate this efficiency quantitatively, primarily because of fundamental differences in mechanical design and biological mimicry between the robot and real fishes. These differences directly affect how energy is stored, transferred, and conserved during locomotion, which is core to swimming efficiency. In real fish, energetic efficiency is strongly enhanced by integrated passive mechanical systems: Structures like skin, muscles, and tendons work in tandem to provide dynamic elasticity and damping (*46*). During tail undulation, for example, fish muscles and tendons absorb energy as the tail flexes and then release this stored energy as the tail reextends to a straight position, effectively recycling energy across each undulation cycle. Even as the amplitude of tail beats (bouts) decays, the fish's tail leverages passive elasticity-damping properties to return to a neutral straight posture without additional energy input, minimizing waste. Although the robot's tail can store limited energy via an elastic thermoplastic polyurethane tube, which deforms to retain small amounts of mechanical energy during tail movement, this capacity pales in comparison with the integrated energy storage systems of a biological fish body. Future work should use soft actuators, such as dielectric elastomer actuators and pneumatic artificial muscles (*49*–*51*), to investigate how to better replicate the viscoelastic properties of real fish.

MATERIALS AND METHODS

Robotic swimming experiments in a lake

We conducted swimming experiments in Port du Bief, a harbor on Lake Léman, chosen for its wide water area that minimized wave disturbances from the robot's movement. We checked weather forecasts beforehand to ensure wind speeds below 5 km/hour, maintaining calm water conditions and stable hovering for the recording drone. We used a DJI Mini-2 drone equipped with a gimbal-stabilized, low-distortion camera (83° view angle) to capture video at 30 frames per second and 4K resolution; we set a 1/1000- to 1/2000-s shutter time and ISO 100 to reduce motion blur. We marked the ZBot with a Swiss cross on the head (for position tracking) and six black dots on the tail joints (for kinematic analysis), adjusting the drone's height on the basis of tracking needs: 14 m for wide-view recording of continuous bouts and 6 m for clear visualization while recording the tail-segmental angles (capturing one or two bouts per recording). We corrected for drone drift (about 0.5 m) using the dock tip as a reference and adjusted the robot's measured velocity to account for left-right water flow by averaging bidirectional velocities [fig. S8 (A and B)]. We measured power consumption of all motors with a calibrated SEN0291 wattmeter (DFRobot, INA219 chip, 50-Hz sampling) connected in series with the servomotors, deducting 3.0 W (constant electronic power for six motors) to isolate movement-related power use. For each parameter setting, we collected 6 to 17 samples for bout-and-glide swimming and 10 to 29 samples (each sample was 5 s) for continuous swimming.

Robotic swimming experiments in lab swimming pool

We performed two sets of lab experiments: swimming experiments to estimate motor efficiency in an indoor pool (6 m by 2 m with 0.3-m water depth) and viscous liquid trials in a smaller family/

infant-sized pool (2.2 m by 1.5 m with 0.2-m water depth). For viscous liquid trials, we tested both bout-and-glide and continuous tail-beating swimming by releasing the robot from one side of the pool and letting it swim freely. In both moderately (213.9 cP) and highly (457.0 cP) viscous liquid, the ZBot could complete a single bout followed by a glide phase that ended in a full stop regardless of parameter settings, so we conducted three trials per setting (consistent performance) to calculate average velocity. For continuous swimming in both viscous liquids, the robot maintained locomotion for more than 6 s, enabling reliable measurement of sustained performance. We used the same power measurement method as in the lake experiments and fixed the DJI Mini-2 drone to the ceiling (propellers disabled) for stable tracking. For motor efficiency estimation, we recorded the input current of each motor by reading its internal states that feed back from each servomotor. We conducted one trial per parameter setting, because these measurements capture internal states with high consistency. We excluded motor 1 from efficiency calculations because of abnormal currents observed under very low–payload conditions (e.g., tail-beating frequency of 0.2 Hz).

Statistical analysis

All figures in this study were generated using Microsoft Excel, except for Fig. 7 (A to C) and figs. S11A and S12A. For these latter figures, where the velocity-CoT relationship is visualized, the trend line was estimated via a two-step process. First, a convex hull algorithm was applied to the dataset to construct the smallest convex polygon enclosing all data points, with points on the polygon's lower boundary selected as fitting candidates. This is a critical step because we used an enumeration method to test tail-beating amplitude and frequency combinations, some of which yielded poor energetic performance, such as abnormally high energy consumption and CoT, that required exclusion to avoid biasing the trend line. Second, a quadratic polynomial was fitted to these lower boundary points using least-squares regression, chosen for its ability to capture the characteristic U-shaped relationship between CoT and velocity (a well-documented pattern in locomotion energetics). The resulting line was plotted to provide a smooth, continuous representation of the velocity-CoT trend, facilitating clearer visualization and interpretation. This two-step method ensures that the trend line is robust, minimizes the influence of outlier points from suboptimal amplitude-frequency combinations, and accurately reflects the dataset's underlying pattern.

Error bars in all figures represent SDs of the measured data, and 95% confidence intervals were calculated on the basis of the SD to further characterize the statistical reliability of the mean values. For each data point displayed with error bars, sample sizes differed by experimental condition: 6 to 17 for bout-and-glide swimming trials conducted in a lake, 3 for bout-and-glide swimming trials conducted in a laboratory swimming pool, and 10 to 29 for continuous tail-beating swimming trials conducted in a lake. The SD values were computed directly using Excel's built-in "STDEV.S" function or the pandas open-source Python library via the pandas.DataFrame.std.() function.

Supplementary Materials

The PDF file includes:
Methods
Figs. S1 to S12
Legends for movies S1 to S6
Legends for data files S1 to S10
References (*52*–*60*)

Other Supplementary Material for this manuscript includes the following:
Movies S1 to S6
Data files S1 to S10

REFERENCES AND NOTES

1. R. Pfeifer, J. Bongard, *How the Body Shapes the Way We Think: A New View of Intelligence* (The MIT Press, 2006).
2. A. J. Ijspeert, Biorobotics: Using robots to emulate and investigate agile locomotion. *Science* **346**, 196–203 (2014).
3. M. B. Orger, G. G. de Polavieja, Zebrafish behavior: Opportunities and challenges. *Annu. Rev. Neurosci.* **40**, 125–147 (2017).
4. E. M. Berg, E. R. Björnfors, I. Pallucchi, L. D. Picton, A. El Manira, Principles governing locomotion in vertebrates: Lessons from zebrafish. *Front. Neural Circuits* **12**, 73 (2018).
5. E. A. Naumann, J. E. Fitzgerald, T. W. Dunn, J. Rihel, H. Sompolinsky, F. Engert, From whole-brain data to functional circuit models: The zebrafish optomotor response. *Cell* **167**, 947–960.e20 (2016).
6. D. L. McLean, M. A. Masino, I. Y. Y. Koh, W. B. Lindquist, J. R. Fetcho, Continuous shifts in the active set of spinal interneurons during changes in locomotor speed. *Nat. Neurosci.* **11**, 1419–1429 (2008).
7. G. Polverino, N. Abaid, V. Kopman, S. Macrì, M. Porfiri, Zebrafish response to robotic fish: Preference experiments on isolated individuals and small shoals. *Bioinspir. Biomim.* **7**, 036019 (2012).
8. T. Wang, Z. Ren, W. Hu, M. Li, M. Sitti, Effect of body stiffness distribution on larval fish–like efficient undulatory swimming. *Sci. Adv.* **7**, eabf7364 (2021).
9. F. Bonnet, R. Mills, M. Szopek, S. Schönwetter-Fuchs, J. Halloy, S. Bogdan, L. Correia, F. Mondada, T. Schmickl, Robots mediating interactions between animals for interspecies collective behaviors. *Sci. Robot.* **4**, eaau7897 (2019).
10. T. Ruberto, V. Mwaffo, S. Singh, D. Neri, M. Porfiri, Zebrafish response to a robotic replica in three dimensions. *R. Soc. Open Sci.* **3**, 160505 (2016).
11. J. C. Marques, S. Lackner, R. Félix, M. B. Orger, Structure of the zebrafish locomotor repertoire revealed with unsupervised behavioral clustering. *Curr. Biol.* **28**, 181–195.e5 (2018).
12. K. E. Severi, R. Portugues, J. C. Marques, D. M. O'Malley, M. B. Orger, F. Engert, Neural control and modulation of swimming speed in the larval zebrafish. *Neuron* **83**, 692–707 (2014).
13. T. Takagi, Y. Tamura, D. Weihs, Hydrodynamics and energy-saving swimming techniques of Pacific bluefin tuna. *J. Theor. Biol.* **336**, 158–172 (2013).
14. G. Wu, Y. Yang, L. Zeng, Kinematics, Hydrodynamics and energetic advantages of burst-and-coast swimming of koi carps (*Cyprinus carpio* koi). *J. Exp. Biol.* **210**, 2181–2191 (2007).
15. G. Li, I. Ashraf, B. François, D. Kolomenskiy, F. Lechenault, R. Godoy-Diana, B. Thiria, Burst–and–coast swimmers optimize gait by adapting unique intrinsic cycle. *Commun. Biol.* **4**, 40 (2021).
16. M.-H. Chung, On burst-and-coast swimming performance in fish-like locomotion. *Bioinspir. Biomim.* **4**, 036001 (2009).
17. C. Ware, R. Arsenault, M. Plumlee, D. Wiley, Visualizing the underwater behavior of humpback whales. *IEEE Comput. Graph. Appl.* **26**, 14–18 (2006).
18. K. Girdhar, M. Gruebele, Y. R. Chemla, The behavioral space of zebrafish locomotion and its neural network analog. *PLOS ONE* **10**, e0128668 (2015).
19. T. D. Wiggin, T. M. Anderson, J. Eian, J. H. Peck, M. A. Masino, Episodic swimming in the larval zebrafish is generated by a spatially distributed spinal network with modular functional organization. *J. Neurophysiol.* **108**, 925–934 (2012).
20. Y. Roussel, S. F. Gaudreau, E. R. Kacer, M. Sengupta, T. V. Bui, Modeling spinal locomotor circuits for movements in developing zebrafish. *eLife* **10**, e67453 (2021).
21. M. Gazzola, M. Argentina, L. Mahadevan, Scaling macroscopic aquatic locomotion. *Nat. Phys.* **10**, 758–761 (2014).
22. J. L. van Leeuwen, C. J. Voesenek, U. K. Müller, How body torque and Strouhal number change with swimming speed and developmental stage in larval zebrafish. *J. R. Soc. Interface* **12**, 20150479 (2015).
23. U. K. Müller, J. L. van Leeuwen, Swimming of larval zebrafish: Ontogeny of body waves and implications for locomotory development. *J. Exp. Biol.* **207**, 853–868 (2004).
24. G. Rajan, J. Lafaye, G. Faini, M. Carbo-Tano, K. Duroure, D. Tanese, T. Panier, R. Candelier, J. Henninger, R. Britz, B. Judkewitz, C. Gebhardt, V. Emiliani, G. Debregeas, C. Wyart, F. D. Bene, Evolutionary divergence of locomotion in two related vertebrate species. *Cell Rep.* **38**, 110585 (2022).
25. K. E. Fouke, Z. He, M. D. Loring, E. A. Naumann, Neural circuits underlying divergent visuomotor strategies of zebrafish and *Danionella* cerebrum. *Curr. Biol.* **35**, 2457–2466.e4 (2025).
26. X. Liu, M. D. Loring, L. Zunino, K. E. Fouke, F. A. Longchamp, A. Bernardino, A. J. Ijspeert, E. A. Naumann, Artificial embodied circuits uncover neural architectures of vertebrate visuomotor behaviors. *Sci. Robot.* **10**, eadv4408 (2025).

27. R. Liu, Q. Yang, Y. Ding, G. Xie, Intermittent swimming demonstrates energy-saving capabilities: Experimental evidence from robotic fish. *Ocean Eng.* **340**, 122335 (2025).
28. D. Weihs, Energetic advantages of burst swimming of fish. *J. Theor. Biol.* **48**, 215–229 (1974).
29. J. C. Liao, Fish swimming efficiency. *Curr. Biol.* **32**, R666–R671 (2022).
30. E. Akoz, K. W. Moored, Unsteady propulsion by an intermittent swimming gait. *J. Fluid Mech.* **834**, 149–172 (2018).
31. Robotis, Robotis e-Manual XM430-W210 (2023); https://emanual.robotis.com/docs/en/dxl/x/xm430-w210/.
32. N. P. Smith, C. J. Barclay, D. S. Loiselle, The efficiency of muscle contraction. *Prog. Biophys. Mol. Biol.* **88**, 1–58 (2005).
33. R. M. Basnet, D. Zizioli, S. Taweedet, D. Finazzi, M. Memo, Zebrafish larvae as a behavioral model in neuropharmacology. *Biomedicine* **7**, 23 (2019).
34. A. Crespi, K. Karakasiliotis, A. Guignard, A. J. Ijspeert, Salamandra robotica II: An amphibious robot to study salamander-like swimming and walking gaits. *IEEE Trans. Robot.* **29**, 308–320 (2013).
35. K.-H. Huang, M. B. Ahrens, T. W. Dunn, F. Engert, Spinal projection neurons control turning behaviors in zebrafish. *Curr. Biol.* **23**, 1566–1573 (2013).
36. A. J. Ijspeert, A. Crespi, D. Ryczko, J.-M. Cabelguen, From swimming to walking with a salamander robot driven by a spinal cord model. *Science* **315**, 1416–1420 (2007).
37. T. R. Thiele, J. C. Donovan, H. Baier, Descending control of swim posture by a midbrain nucleus in zebrafish. *Neuron* **83**, 679–691 (2014).
38. M. J. McHenry, G. V. Lauder, The mechanical scaling of coasting in zebrafish (*Danio rerio*). *J. Exp. Biol.* **208**, 2289–2301 (2005).
39. A. Jouary, M. Haudrechy, R. Candelier, G. Sumbre, A 2D virtual reality system for visual goal-driven navigation in zebrafish larvae. *Sci. Rep.* **6**, 34015 (2016).
40. L. Xu, N. N. Guan, C.-X. Huang, Y. Hua, J. Song, A neuronal circuit that generates the temporal motor sequence for the defensive response in zebrafish larvae. *Curr. Biol.* **31**, 3343–3357 (2021).
41. T. Kohashi, Y. Oda, Initiation of Mauthner-or non-Mauthner-mediated fast escape evoked by different modes of sensory input. *J. Neurosci.* **28**, 10641–10653 (2008).
42. K. Ampatzis, J. Song, J. Ausborn, A. El Manira, Separate microcircuit modules of distinct v2a interneurons and motoneurons control the speed of locomotion. *Neuron* **83**, 934–943 (2014).
43. S. Li, Z. Wu, J. Wang, Y. Feng, M. Tan, J. Yu, Towards efficient intermittent-propulsion mode of a novel bioinspired underwater vehicle. *IEEE Trans. Intell. Veh.* **10**, 346–358 (2025).
44. J. L. Kendall, K. S. Lucey, E. A. Jones, J. Wang, D. J. Ellerby, Mechanical and energetic factors underlying gait transitions in bluegill sunfish (*Lepomis macrochirus*). *J. Exp. Biol.* **210**, 4265–4271 (2007).
45. S.-J. Fu, Z. Peng, Z.-D. Cao, J.-L. Peng, X.-K. He, D. Xu, A.-J. Zhang, Habitat-specific locomotor variation among Chinese hook snout carp (*Opsariichthys bidens*) along a river. *PLOS ONE* **7**, e40791 (2012).
46. D. M. Bramble, D. E. Lieberman, Endurance running and the evolution of *Homo*. *Nature* **432**, 345–352 (2004).
47. D. F. Hoyt, C. R. Taylor, Gait and the energetics of locomotion in horses. *Nature* **292**, 239–240 (1981).
48. S. H. Devoto, E. Melançon, J. S. Eisen, M. Westerfield, Identification of separate slow and fast muscle precursor cells in vivo, prior to somite formation. *Development* **122**, 3371–3380 (1996).
49. S. M. Mirvakili, D. Sim, I. W. Hunter, R. Langer, Actuation of untethered pneumatic artificial muscles and soft robots using magnetically induced liquid-to-gas phase transitions. *Sci. Robot.* **5**, eaaz4239 (2020).
50. B. Kalita, A. Leonessa, S. K. Dwivedy, A review on the development of pneumatic artificial muscle actuators: Force model and application. *Actuators* **11**, 288 (2022).
51. G. Li, X. Chen, F. Zhou, Y. Liang, Y. Xiao, X. Cao, Z. Zhang, M. Zhang, B. Wu, S. Yin, Y. Xu, H. Fan, Z. Chen, W. Song, W. Yang, B. Pan, J. Hou, W. Zou, S. He, X. Yang, G. Mao, Z. Jia, H. Zhou, T. Li, S. Qu, Z. Xu, Z. Huang, Y. Luo, T. Xie, J. Gu, S. Zhu, W. Yang, Self-powered soft robot in the Mariana Trench. *Nature* **591**, 66–71 (2021).
52. S. Falcinelli, S. Picchietti, A. Rodiles, L. Cossignani, D. L. Merrifield, A. R. Taddei, F. Maradonna, I. Olivotto, G. Gioacchini, O. Carnevali, *Lactobacillus rhamnosus* lowers zebrafish lipid content by changing gut microbiota and host transcription of genes involved in lipid metabolism. *Sci. Rep.* **5**, 9336 (2015).
53. V. Mwaffo, P. Zhang, S. R. Cruz, M. Porfiri, Zebrafish swimming in the flow: A particle image velocimetry study. *PeerJ* **5**, e4041 (2017).
54. Z. Zhao, G. Li, Q. Xiao, H.-R. Jiang, G. M. Tchivelekete, X. Shu, H. Liu, Quantification of the influence of drugs on zebrafish larvae swimming kinematics and energetics. *PeerJ* **8**, e8374 (2020).
55. J. Chang, M. Wang, W. Gui, Y. Zhao, L. Yu, G. Zhu, Changes in thyroid hormone levels during zebrafish development. *Zoolog. Sci.* **29**, 181–184 (2012).
56. P. R. Bandyopadhyay, Trends in biorobotic autonomous undersea vehicles. *IEEE J. Ocean. Eng.* **30**, 109–139 (2005).
57. T. C. Gillmer, B. Johnson, *Introduction to Naval Architecture* (Springer, 1982).
58. K. Karakasiliotis, R. Thandiackal, K. Melo, T. Horvat, N. K. Mahabadi, S. Tsitkov, J.-M. Cabelguen, A. J. Ijspeert, From cineradiography to biorobots: An approach for designing robots to emulate and study animal locomotion. *J. R. Soc. Interface* **13**, 20151089 (2016).
59. P. Moreno, R. Nunes, R. Figueiredo, R. Ferreira, A. Bernardino, J. Santos-Victor, R. Beira, L. Vargas, D. Aragão, M. Aragão, "Vizzy: A humanoid on wheels for assistive robotics," in *Robot 2015: Second Iberian Robotics Conference*, L. P. Reis, A. P. Moreira, P. U. Lima, L. Montano, V. Muñoz-Martinez, Eds. (Springer International Publishing, 2016), pp. 17–28.
60. G. Metta, L. Natale, F. Nori, G. Sandini, D. Vernon, L. Fadiga, C. von Hofsten, K. Rosander, M. Lopes, J. Santos-Victor, A. Bernardino, L. Montesano, The *iCub* humanoid robot: An open-systems platform for research in cognitive development. *Neural Netw.* **23**, 1125–1134 (2010).

Acknowledgments: We thank A. Anastasiadis, L. Paez, M. Mutlu, Q. Fu, A. Gupta, and S. Fiaux for support in the robotic development; M.-E. Busse-Grawitz for useful discussions on motor efficiencies, and F. Gallaire, L. Molefe, and M. Landry for access to the viscometer and help with viscosity measurements. X.L. specially thanks K. Hosoda, J. Santos-Victor, and R. Pfeifer for supervision in robot development, inspiration in organization, and guidance on embodiment intelligence; G. Valentin from Center of PhenoGenomics, EPFL fish facility for providing the videos and photos of zebrafish larvae; T. Mauro for inspiration and kindness; and the yacht owners at Port du Bief (Lake Léman) for allowing us to perform the experiments in the harbor. **Funding:** This work was supported by the European Research Council 951477, FCT PhD Grant PD/BD/135152/2017, LARSyS FCT funding (DOI: 10.54499/LA/P/0083/2020, 10.54499/UIDP/50009/2020, and 10.54499/UIDB/50009/2020); E.A.N. was supported by the Whitehall Foundation, Alfred P. Sloan Foundation, and the NIH BRAIN initiative (award number RF1NS128895-01). The content is solely the authors' responsibility and does not necessarily represent the official views of the NIH. **Author contributions:** X.L., F.A.L., E.A.N., and A.J.I. conceptualized the project; X.L., F.A.L., L.Z., L.G., S.I.B., L.R.S., A.C., and A.G. developed the robot; X.L., F.A.L., L.G., L.R.S., L.Z., and G.B. performed the experiments; X.L., L.G., and A.J.I. analyzed the data; X.L., A.B., E.A.N., and A.J.I. supervised the project; X.L., L.G., G.B., and A.J.I. wrote the original manuscript; X.L., L.G., G.B., A.B., E.A.N., and A.J.I. reviewed and edited the manuscript. **Competing interests:** The authors declare that they have no competing interests. **Data, code, and materials availability:** Materials were commercially available. All data needed to evaluate the conclusions in the paper are present in the paper or the Supplementary Materials. The code for data processing can be found at https://doi.org/10.5281/zenodo.17978787.

Submitted 6 March 2025
Accepted 23 December 2025
Published 28 January 2026
10.1126/scirobotics.adw7868

Correction (11 February 2026): The Acknowledgments were updated to correct the spelling of S. Fiaux and to add F. Gallaire, L. Molefe, and M. Landry.

Science Robotics

Energy efficiency and neural control of continuous versus intermittent swimming in a fishlike robot

Xiangxiao Liu, François A. Longchamp, Luca Zunino, Louis Gevers, Lisa R. Schneider, Selina I. Bothner, André Guignard, Alessandro Crespi, Guillaume Bellegarda, Alexandre Bernardino, Eva A. Naumann, and Auke J. Ijspeert

Sci. Robot. **11** (110), eadw7868. DOI: 10.1126/scirobotics.adw7868

Science Robotics (ISSN 2470-9476) is published by the American Association for the Advancement of Science. 1200 New York Avenue NW, Washington, DC 20005. The title *Science Robotics* is a registered trademark of AAAS.